Modeling the Spectral Energy Distribution of Mrk 421

Randall L. Oglesby

Advisor, Dr. Luis C. Reyes

Department of Physics

California Polytechnic State University

San Luis Obispo

May, 2013

Contents

1 Abstract

Blazars are astronomical objects thought to be powered by the release of gravitational energy by accretion of material into a supermassive black hole located in the central region of the host galaxy. Some AGN present strong relativistic outflows in the form of jets, with blazars being the particular subset whose jets are aligned with our line of sight. Even though blazars account for only a small fraction of all AGN, they are the dominant class source in the high-energy sky. In this thesis we study the spectral energy distribution of Mrk 421, a prototypical blazar. Using publicly available numerical code we consider its emission in the context of a Synchrotron Self-Compton model in order to constrain physical parameters of the source.

2 A Background on Blazars and Blazar Theory

2.1 Blazars

Active Galactic Nuclei (AGN) are galaxies that contain a supermassive black hole and an accretion disk. As a result of the large release of energy during accretion, AGN have a high luminosity over the entire electromagnetic spectrum. The type of AGN that is of interest to this paper are radio loud AGN; or AGN that have relativistic jets perpendicular to the accretion disk (also known as quasars) as shown in (Figure1). Blazars are quasars in which one of the relativistic jets are pointed in our direction.

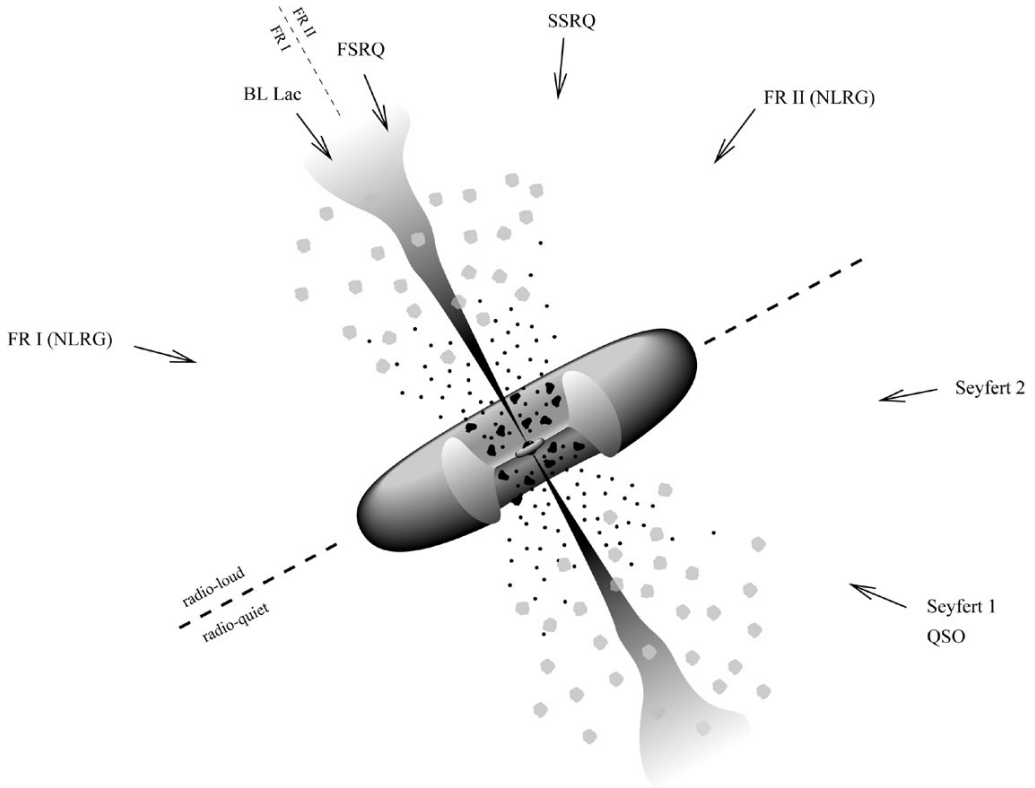

Figure 1: Shown is a depiction of an AGN. In the center is a black hole with an accretion disk, surrounded by a large torus of slow moving dust. Perpendicular to the plane of the accretion disk are relativistic jets. The figure is marked with different classifications of AGN depending on the orientation to the viewer. Blazars are oriented so that we are looking down one of the jets, towards the black hole at the center [1].

The accretion disk is made of ionized plasma and is surrounded by a torus of slow moving dust. The relativistic jet streams emit photons with energies reaching into the TeV regime ([2] and references therein). The acceleration mechanism for ultra relativistic electrons in the jet streams has yet to be confirmed, but most models assume the injection of a power-law distribution of electrons up to a certain Lorentz factor [3].

Blazars are split into two categories: Flat-spectrum radio quasars (FSRQ's) and BL Lacs. FSRQ's contain strong emission lines, are bright and tend to be father away($z > 1$), while BL Lac objects have no emission lines, are dimmer and tend to be closer($z < 1$). Emission lines would indicate a presence of gas clouds as shown in Figure 1; therefore an absence of emission lines indicate an absence of gas clouds. The BL Lac object Mrk 421 will be examined in this paper.

2.2 Physical Processes in Blazars

The Spectral Energy Distribution (SED) from a Blazar consists of two broad non-thermal peaks: one at low energies (UV through X-rays) and another at higher energies (X-rays through γ-rays) as seen in Figure 2.

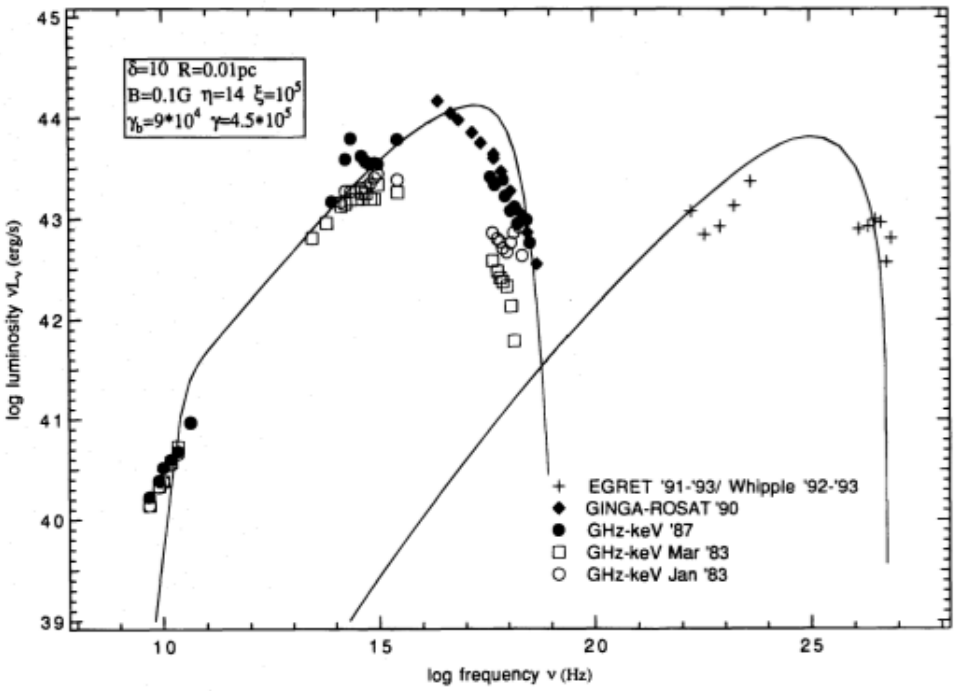

Figure 2: Model fit from early observations of Mrk 421. Best fit model parameters are shown within the figure. The low energy bump is due to synchrotron radiation, and the high energy peak has no definite explanation [4].

The two separate peaks indicate different emission mechanisms: the low energy peak is believed to be caused by synchrotron radiation from non-thermal, ultra-relativistic electrons while the high energy peak has no definite explanation [2]. One of the most widely accepted theories for the second peak is the Synchrotron Self Compton model (SSC). It is the SSC model that we will explore in further detail in this paper.

2.2.1 Synchrotron Radiation

Synchrotron radiation occurs when ultra-relativistic electrons are in the presence of strong magnetic fields. The magnetic fields cause the electrons to follow a spiral path, projecting radiation into a cone of angle θ with critical frequency ω_c :

$$\theta \approx \frac{mc^2}{E} \tag{1}$$

$$\omega_c = \frac{3}{2}\frac{eB}{mc}\gamma^2 sin\phi. \tag{2}$$

where ϕ is the angle between the direction of the magnetic field line and the electron's path. E is the energy of the electron, B is the magnetic field, m is the mass of an electron, c is the speed of light, and γ is the Lorentz factor [5].

Synchrotron radiation extends over a wide range of frequencies, but it peaks at a value given by,

$$\nu_s = \frac{3}{2}\gamma^2 \times \frac{eB}{2\pi m \sin\theta}. \tag{3}$$

The low energy bump is caused by synchrotron radiation, and is widely accepted as such.

2.2.2 Inverse Compton Radiation

The scattering of a photon off of an electron is known as Compton scattering. Compton scattering is typically viewed in the reference frame of the electron, where photons transfer most of their energy to the electron; while in inverse Compton scattering, relativistic electrons transfer most of their energy to photons. Inverse Compton regards the collision between a relativistic electrons and soft photons of distribution,

$$q(\epsilon) = \int d\epsilon_o n(\epsilon_o) \int d\gamma N(\gamma) C(\epsilon, \gamma, \epsilon_o), \tag{4}$$

where $n(\epsilon_o)$ is the number density of low energy photons(soft photons) per energy interval, ϵ is the allowed kinematic range, and $N(\gamma)$ represents the electron distribution, where the Compton kernel is,

$$C(\epsilon, \gamma, \epsilon_o) = \frac{2\pi r_e^2 c}{\gamma^2 \epsilon_o}\left[2\kappa + (1+2\kappa)(1-\kappa) + \frac{(4\epsilon_o\gamma\kappa)^2}{2(1+4\epsilon_o\gamma\kappa}(1-\kappa)\right] \tag{5}$$

and

$$\kappa = \frac{\epsilon}{4\epsilon_o\gamma(\gamma-\epsilon)}. \tag{6}$$

The electron transfers most of its energy to the photon, often boosting it into the gamma regime [6].

This cross section can be calculated exactly using quantum electrodynamics. For practical purposes however, it is sufficient to say that when the energy of the electron is below mc^2 in the center-of-momentum frame of the electron-photon system, the cross section is approximately constant given by:

$$\sigma \sim \sigma_t = \frac{e^4}{6\pi m_e^2 \epsilon_0^2 c^4} = 6.6524 \times 10^{-25} cm^2 \tag{7}$$

which is commonly referred to as the Thomson cross section and the interaction is said to take place in the Thomson regime. If, in the other hand, the electron energy is above mc^2 the cross section asymptotically decreases with energy as:

$$\sigma \sim \frac{3}{8}\sigma_t \times \frac{mc^2}{h\nu} \times \left(1 + 2ln\frac{h\nu}{mc^2}\right) \tag{8}$$

where ν is the frequency of the photon and h is Planck's constant. This is called the Kline-Nishina regime.

2.2.3 Photopion Production

Certain interactions, like cosmic ray proton collisions with gas nuclei produce large amounts of pions. The neutral pions created are unstable and decay into $\gamma - ray$ photons with an approximate energy of 70 MeV. Due to the momentum of the initial pions, the observed $\gamma - ray$ bump can be doppler shifted to higher energies by a doppler factor of δ [7]:

$$\delta = [\Gamma(1 - \beta cos\theta)]^{-1} \tag{9}$$

Where Γ is the Lorentz factor, and $\beta = \mathrm{v}_s/c$. Similarly, $\gamma - rays$ are produced when high energy protons collide with photons, a process called photopion production:

$$\begin{aligned} p + \gamma &\rightarrow \pi^0 + p \\ &\rightarrow \pi^+ + n \\ &\rightarrow e^- + e^+ + p \end{aligned}$$

The pion produced decays into photons which may undergo inverse Compton scattering with the produced pair of electrons ([2] and references therein).

2.3 Blazar Emission Models

2.3.1 Leptonic Models

The leptonic model assumes that electrons and positrons are the primary particles accelerated in the jets of a blazar. When protons are not accelerated to energies high enough to reach the threshold for photopion production, then ultra-relativistic electrons dominate high energy emission [4]. While there is no clear source of soft photons, two main theories have emerged, synchrotron self compton and external compton.

2.3.1.1 Synchrotron Self Compton Synchrotron Self Compton (SSC) is a process common in blazars in which high energy gamma rays are produced by inverse Compton scattering off the same population of ultra-relativistic electrons that are producing synchrotron radiation. These synchrotron photons then inverse Compton scatter off the same population of relativistic electrons that created them [2]. The characteristic high-energy frequency, or "Compton" frequency, ν_c, is related to the magnetic field, B, and the electron energy, E, by

$$\nu_c \propto \nu_s \times E_e^2 \approx B \times E_e^4. \tag{10}$$

2.3.1.2 External Compton External Compton (EC) is a very similar process to Synchrotron Self Compton, but assumes an external source of photons. Photons of low energy could originate in the accretion disk, emission line regions, or the torus, which then scatter into the jet. Similarly, synchrotron photons that are created in the jet and leave could re-scatter back into the jet by broad-line emission clouds. Photons coming directly from the accretion disk will travel into the jet where they will come in contact with relativistic electrons and undergo Inverse Compton scattering [6].

Both SSC and EC photons are believed to be present in the blazar jets, but their presence varies with different classes of blazars. BL Lacs are believed to have less matter in their central regions, and thus are expected to have a greater SSC presence [2].

2.3.2 Hadronic Models

The hadronic model assumes that protons are being accelerated to energies high enough to reach the threshold for photopion production. In order for these protons to be accelerated to high enough energies, an extremely powerful magnetic field must be present (10's of Gauss). The decay of these protons create cascades in which synchrotron radiation will occur among the protons, muons, and mesons. This synchrotron radiation is responsible for the high energy bump, where synchrotron radiation among the electrons remains the source for the low energies[4].

3 The Spectral Energy Distribution of Mrk 421

3.1 Markarian 421

In 1992, Mrk 421 was discovered as a source of TeV gamma-rays by the Whipple Observatory [8] and it was the first extragalactic source observed at such high energy. Due to its close proximity, $z = 0.031$, it is the most widely studied TeV emitting blazar.

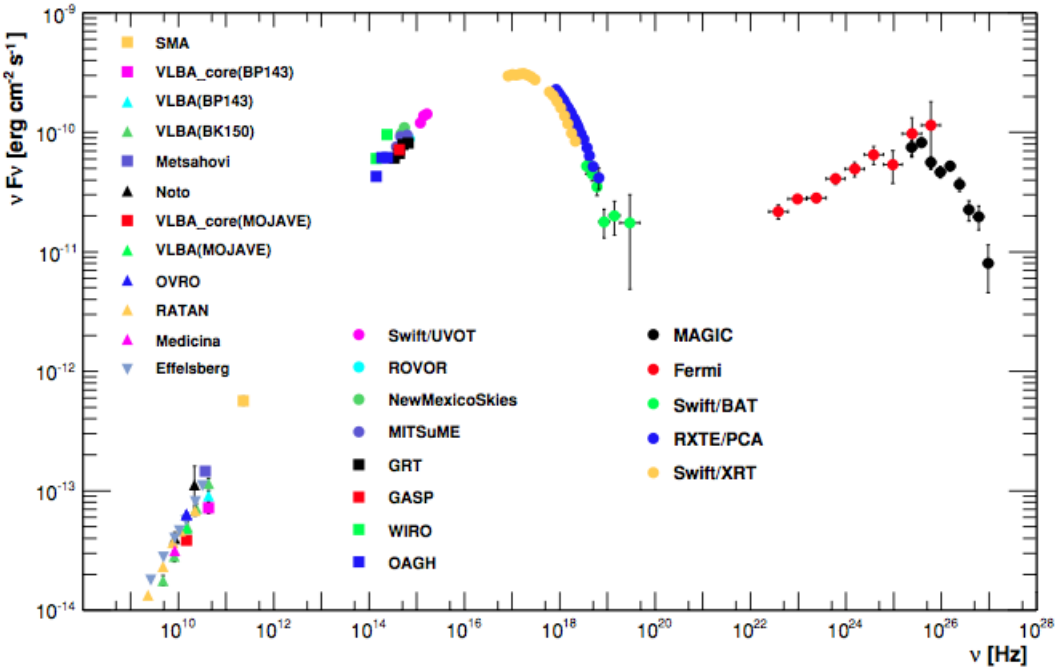

Figure 3: This SED of Mrk 421 is the most complete set of observations ever gathered for this object taken during the multifrequency campaign in January 2009. The corresponding instruments used are shown in the legend [9].

Markarian 421 (Mrk 421) is a unique gamma-ray-emitting BL Lac object located at RA: 11:04:27.3 Dec: 38:12:31. It is a strong radio source with no spectroscopic absorption lines, meaning the source of its brightness it not starlight. The spectrum has two large broadband components; the first component extends from radio through x-rays, while the second high energy extends into the TeV energy regime. The gamma ray emission extends from 50 MeV to the TeV range.

Even though Mrk 421 is the most widely studied TeV blazar, new observations by several radio and optical telescopes, the Swift and Fermi satellites, and MAGIC and VERITAS have provided much more data on the source, allowing new, more accurate studies to be completed. The average SED of Mrk 421, resulting from a long multi-wavelength campaign in 2009, is shown in Figure 3. This is the most complete SED ever collected for Mrk 421. At gamma-ray frequencies, the combination of GeV and TeV data allows, for the first time, constraints on the high energy bump with complete coverage.

3.2 Parameters and Observables

The SSC model assumes that radiation is produced in a single zone of the jet (of radius R), moving at an angle θ with respect to the observer's line of sight. As electron energy increases, the slope of the electron spectrum increases. This can be approximated with a broken power law (with indices $n_1 < 3$ and $n_2 > 3$) above and below the break energy respectively:

$$N(\gamma) = \begin{cases} K\gamma^{-n_1} \text{if} & \gamma < \gamma_b \\ K\gamma_b^{n_2-n_1}\gamma^{-n_2} \text{if} & \gamma > \gamma_b \end{cases}. \tag{11}$$

We can specify the model with seven parameters: the magnetic field B, the size of the emission region R, the doppler factor delta, the slopes n_1 and n_2, the break energy of the electron distribution γ_b, and the integrated electron density K (acting as an overall normalization factor). Available data on Mrk 421 can be used to derive "observable" quantities: α_1 and α_2, frequencies of the synchrotron and SSC peaks ν_s and ν_c, and the peak luminosities $L_s(\nu_s)$ and $L_c(\nu_c)$, and the minimum timescale of variation t_{var} [7].

Relations between observables and model parameters allow us to narrow down the input parameters for the theoretical model database. We will establish a $B - \delta$ parameter space that will allow us to constrain the input parameters for our code [7].

3.3 Thomson Regime

When the inverse Compton limit lies in the Thomson regime, it will be dominated by photons at frequency $\nu_c = (4/3)\gamma_b^2 \nu_s' \delta$, where $\nu_s = \nu_s' \delta$. By combining and reducing the equations, we see that the peak frequencies of the SED are correlated and give the ratio

$$\gamma_b = \left(\frac{3\nu_c}{4\nu_s}\right)^{1/2}. \tag{12}$$

When the synchrotron frequency is averaged over the SED for an electron of γ_b, then

$$\nu_s = 3.7 \times 10^6 \gamma_b^2 B \frac{\delta}{1+z}. \tag{13}$$

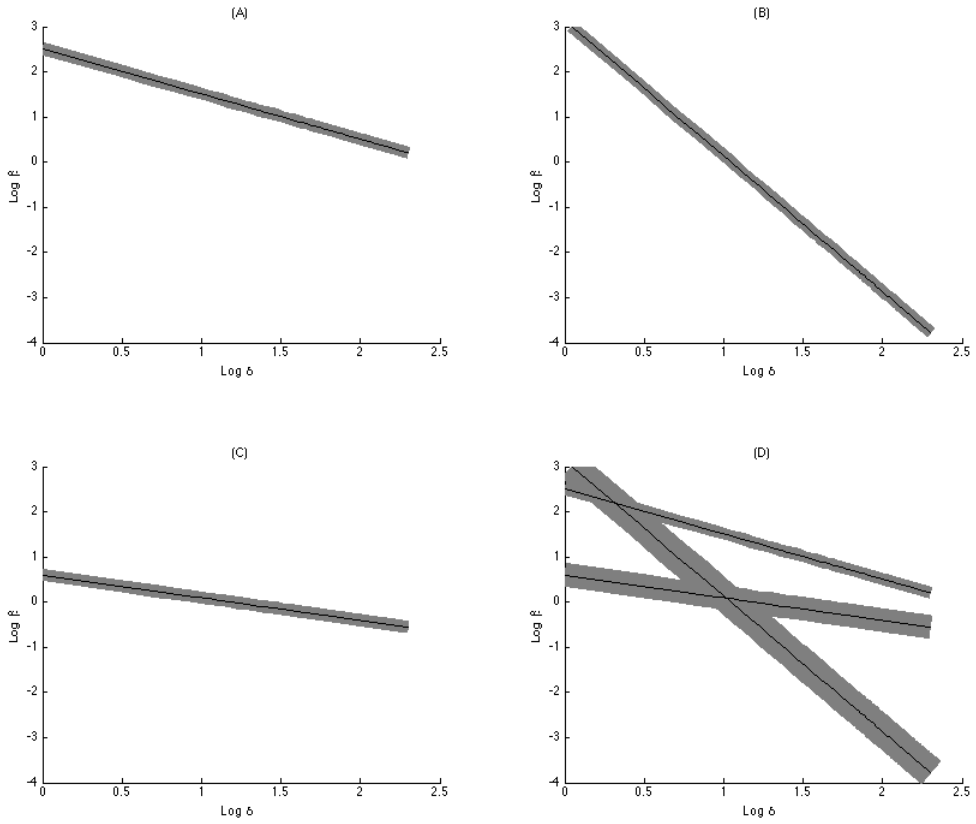

Figure 4: Constraints on the Thomson regime parameter space for Mrk 421 . Region A represents the peak frequency constraint from eq.(14.) Region B represents the luminosity constraint from (eq. 17.) Region C represents (eq. 18). In all regions, uncertainty is taken into account for time variation and β_{esc}.

Using this, we can rearrange the terms, creating a $B-\delta$ parameter space that is limited to observable quantities:

$$B\delta = (1+z)\frac{\nu_s^2}{2.8\times10^6\nu_c}. \tag{14}$$

This $B-\delta$ parameter space gives plot (A) shown in Figure 4. This line shows $B-\delta$ combinations that satisfy the ratio between the peak frequencies.

The peak luminosities are also correlated and can be describes as the area under the peaks. The luminosity is thus given by

$$L_{s,c} = f(\alpha_1,\alpha_2)\nu_{s,c}L_{s,c}(\nu_{s,c}) \tag{15}$$

where $\alpha_{1,2}$ give the slope of the data on each side of the peaks and $f(\alpha_1,\alpha_2)$ is given by

$$f(\alpha_1,\alpha_2) = \frac{1}{1-\alpha_1} + \frac{1}{\alpha_2-1}. \tag{16}$$

We are then able to write the expression for the $B-\delta$ parameter space as

$$B\delta \geq (1+z)\left\{\frac{2[\nu_s L_s(\nu_s)]^2 f(\alpha_1,\alpha_2)}{c^3 t_{var}^2 \nu_c L_c(\nu_c)}\right\}^{1/2}. \tag{17}$$

This $B-\delta$ parameter space is shown in plot (B) Figure 4. This $B-\delta$ line shows combinations that satisfy the relation between the peak luminosities.

When cooling is dominated by the synchrotron process, we can relate $B-\delta$ in terms of observable quantities:

$$B\delta^{1/2} > \left[\frac{5\times10^8(\nu_s/\nu_c)^{1/2}(1+z)}{t_{var}}\right]^{1/2}\beta_{esc}^{1/2} \tag{18}$$

where β_{esc} is the electron escape velocity.

3.4 Klein-Nishina Regime

The constraints from the previous section were obtained assuming that the electron and the photon are interacting in the Thomson regime, which has a constant cross section and thus simple relationships between the synchrotron and Compton peak frequencies. Analytical calculations are harder in the Klein-Nishina regime because the cross section changes with energy.

It is important to remember that the scattering of photons off electrons becomes less efficient in the Klein-Nishina regime. As we approach this regime, the interaction of the highest energy electrons of the distribution and the highest energy synchrotron photons will produce less gamma-rays.

A full analytical treatment of this problem is beyond the scope of this work. It suffices to say that the following constraints from Tavecchio et al. are useful approximations and that the numerical code by Krawczynski et al. uses the full cross section (including KN effects when appropriate.)

For synchrotron frequencies above some critical value, we have the onset of the Klein-Nishina regime and a rapid decrease of the cross section. Thus, the Compton peak is determined by this maximum frequency. For an electron population with a broken power law distribution, the following relation applies between the Compton peak and the break energy:

$$\nu_c = \nu_c^{'} \simeq \frac{mc^2}{h}\gamma_b g(\alpha_1,\alpha_2)\frac{\delta}{1+z} \tag{19}$$

where

$$g(\alpha_1,\alpha_2) = \exp\left[\tfrac{1}{\alpha_1-1}+\tfrac{1}{2(\alpha_2-\alpha_1)}\right]. \tag{20}$$

Which results in the following contraint from B and δ:

$$\frac{B}{\delta} = \frac{\nu_s}{\nu_c^2}\left(\frac{mc^2}{h}\right)^2\frac{g(\alpha_1,\alpha_2)^2}{3.7\times10^6}\frac{1}{z+1} \tag{21}$$

Similarly, in the KN regime, the power of the Compton peak is significantly reduced due to the less efficient cross section. Indeed, only synchroton photons below the limiting frequency mentioned above will contribute. The following is a constraint derived from the ratio of the Compton peak to the Synchrotron peak in the KN regime:

$$B\delta^{(2+\alpha_1)} > (1+z)^{\alpha_1}\left[\frac{g(\alpha_1,\alpha_2)}{\nu_c\nu_s}\right]^{(1-\alpha_1)/2} \times \left\{\frac{2[\nu_s L_s(\nu_s)]^2 f(\alpha_1,\alpha_2)}{c^3 t_{var}^2 \nu_c L_c(\nu_c)}\right\}^{1/2}\left(\frac{3mc^2}{4h}\right)^{1-\alpha_1} \tag{22}$$

Compton cooling is less important than synchrotron cooling, but when it occurs in the KN regime, γ_b must be taken from equation 19 instead of equation 12. This gives:

$$B\delta^{6/(1-\alpha_1)} = \xi(\alpha_1,\alpha_2)\left[\frac{\nu_s L_s(\nu_s) f(\alpha_1,\alpha_2)}{t_{var}\beta_{esc}}\right]^{1/(1-\alpha_1)} \times [\nu_c(1+z)]^{(3\alpha_1-2)/(1-\alpha_1)} \tag{23}$$

Equations 21, 22 and 23 are shown in a $B-\delta$ parameter space in Figure 5.

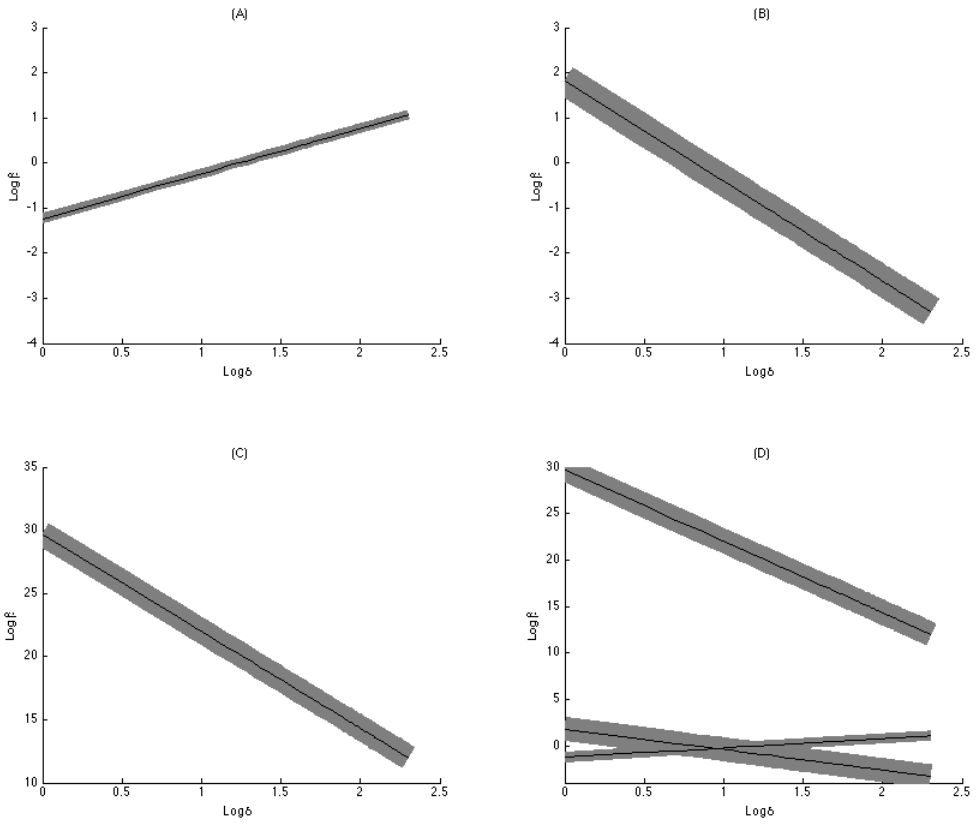

Figure 5: Constraints on the Kline-Nishina regime parameter space for Mrk 421 . Region A represents the peak frequency constraint from eq.(21.) Region B represents the luminosity constraint from (eq. 22.) Region C represents (eq. 23). In all regions, uncertainty is taken into account for time variation and β_{esc}.

3.5 Combined Constraints

By using the $B-\delta$ parameter spaces created in the above plots, the input parameters can be narrowed down to $B-\delta$ combinations that fall closely to the intersection of the lines. In the Kline-Nishina regime, B values are narrowed down between .049 T and 7.389 T, while the δ values are narrowed down between 4.29 T and 5.14 T.

4 Spectral Modeling

4.1 SSC Numerical Model

Krawczynski et al. [3] has done extensive research on blazars and has a publicly available code that, with input parameters, will produce an SED (assuming a leptonic model). Using this publicly available code, a database of model SED's was created for comparison to the data. By comparing the model curves to the data, a best fit curve is found, which will in turn provide the physical parameters of Mrk 421 at the time of observation. Below is a list of the parameters that can be found using this SSC numerical model.

Symbol	Parameter
z	Redshift
γ	Bulk Lorentz factor of emitting blob
θ	Angle(degree) between the jet axis and the line of sight in the observer frame
B	Strength of tangled magnetic field in the jet stream in T
R	Radius of emission volume in m
$W_{p,soll}$	jet-frame number density of electrons in cm^{-3}
$log(E_{min})$	logarithm of minimum electron energy in eV
$log(E_{max})$	logarithm of maximum electron energy in eV
$log(E_{break})$	logarithm of electron energy at break of powerlaw (from $p = p_1$to $p = p_2$)
p_1	differential spectral index of electron spectrum from $E_{min}$to E_{break}
p_2	differential spectral index of electron spectrum from $E_{break}$to E_{max}

Table 1: Listed are the free parameters used in the SSC numerical Model.

4.2 Parameter Sweep

A set of scripts were written in PERL language in order to execute the numerical code of Krawczynski et al. with different physical parameters. A database of over 2000 SSC curves was compiled using the computer cluster of the physics department, with each curve taking around 2-3 minutes to run.

After the database of model SSC curves was completed, they were compared to the data in order to find the one with the best fit. To do so, a phase space is created and a grid search is performed. For every model generated, a calculated normalized sum of the squared differences(eq 24) is determined to find the curve closest to the data.

$$\chi^2 = \frac{(Observed - Expected)^2}{Expected} \tag{24}$$

4.3 Best Model

After completing the calculation of the χ^2 value for each model curve, it was determined that physical parameters corresponding to the Klein-Nishina regime fit well and that paremeters corresponding to the Thomson regime failed to match the data for Mrk 421. The best fit parameters are shown in Table 2, accompanied by the best fit curve compared to the data in Figure 6.

Symbol	Parameter	Value
γ	Bulk Lorentz factor	11
B	Strength of tangled magnetic field	$10^{-5}\ T$
R	Radius of emission	$10^{14}\ m$
ED	Electron Density	$2 \times 10^{17}\ cm^{-3}$
E_{min}	Minimum electron energy	$10^{4}\ eV$
E_{max}	Maximum electron energy	$10^{14} eV$
E_{break}	Break energy	$10^{10.9}\ eV$
n_1	Index 1	2.2
n_2	Index 2	4.4

Table 2: Shown are the best fit parameters acquired by the parameter sweep.

Figure 6 shows the best fit model curve in comparison to the data from Mrk 421. The structure of the best fit model curve does not perfectly match the data. It's important to recognize that the one-zone SSC is an oversimplified picture of a complex system; the obtained fit is useful however, it allows us to determine the physical parameter that dominate the source overall.

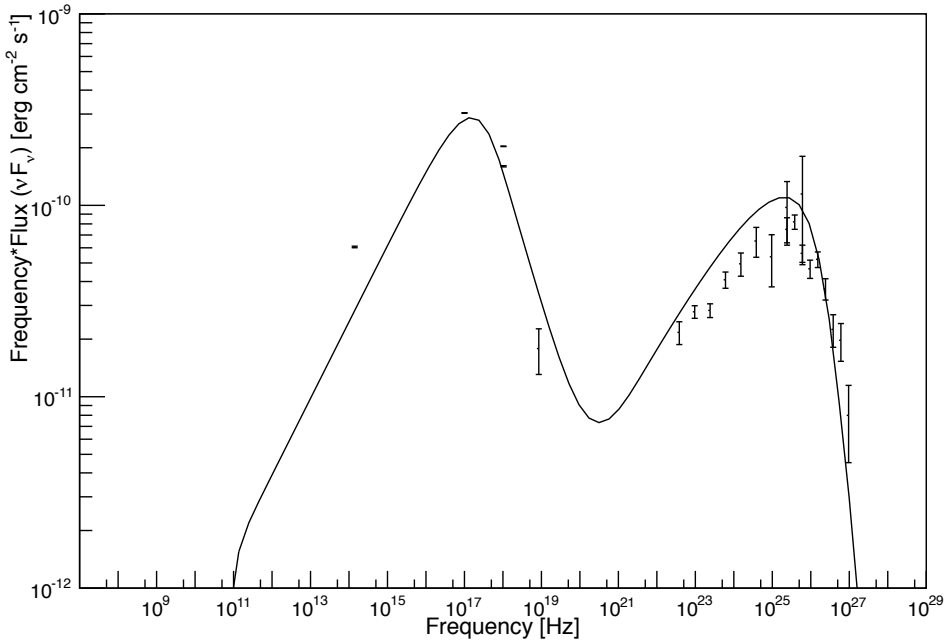

Figure 6: Shows the model curve superimposed over the data. While not a perfect match, it allows the dominating physical parameters to be determined.

5 Summary and Conclusions

This senior thesis studies the spectral energy distribution of Mrk 421 in the context of a Synchrotorn Self-Compton (SSC) scenario. By developing a computational strategy that utilizes a publicly available code,

a database of theoretical SSC model curves was created which could be compared to data in order to determine the physical parameters of a blazar. The size of the database was reduced a priori by using physical constraints from Tavecchio et al [7]. This method was then successfully used to find a best fit curve to determine the physical parameters of Mrk 421 at the time of observation. These results show that for the set of data used, the KN regime was a best fit, other results include: a magnetic field of 10^{-5} T, an emission zone of 10^{14} cm, a Bulk Lorentz factor of 11, minimum and maximum electron energies of 10^4 and 10^{14} eV respectively, a break energy of 2×10^{10}eV, and spectral indices below and above the break energy of 2.2 and 4.4.

The tools developed in this senior project will allow for future students and for members of the VERITAS collaboration to continue the study of Mrk 421 and other blazars. It will assist in the determination of how Mrk 421 changes with time, including during high energy flares. If the magnetic field changes by several orders of magnitude, the code will provider what other parameters changed, potentially leading to a new and better physical understanding of how the physics inside a blazar works.

In conclusion, this senior project thesis is a modest but significant contribution to the field of gamma-ray astrophysics, as we try to better understand the mechanisms that drive the gamma-ray emission of blazars.

References

[1] Urry, C. M., and Padovani, P., PASP(1995), 107, 803

[2] Reyes, L. C., PhD Thesis(2007), University of Maryland, College Park

[3] Krawczynski, H., et al., "Multiwavelength Observations of Strong Flares from the TeV Blazar 1ES 1959+650",ApJ(2004),601:151-164.

[4] Markus Böttcher. Modeling the Emission Processes in Blazars. Astrophys Space Sci (2007), 309: 95–104

[5] T.C.Weekes. Very High Energy Gamma-Ray Astronomy. IOP Publishing Ltd(2003).

[6] Susumu Inoue and Fumio Takahara. Electron Acceleration and Gamma-Ray Emission from Blazars. ApJ(1996), 462: 555-564.

[7] Tavecchio, Maraschi, Ghisellini. Constraints on the Physical Parameters of the TeV Blazars. The ApJ(1998), 509:608-619.

[8] Gaidos, J. A., et al., Nature(1996), 383, 319

[9] A. A. Abdo. Fermi Large Area Telescope Observations of Markarian 421: The Missing Piece of its Spectral Energy Distribution.